



Anti-aliasing Technique for Inferring Dispersion of Short-wavelength Instabilities in Electric Propulsion Devices

Miron F. Liu* and Benjamin A. Jorns†
University of Michigan, Ann Arbor, Michigan, 48105

An anti-aliasing analysis technique for inferring wave dispersion that leverages Bayesian inference is compared to a standard two-point correlation Beall analysis using toy numerical data to simulate propagating plasma waves. The theoretical underpinnings of the algorithm and methodology for generating toy numerical data are presented. Dispersion plots produced by applying the algorithm to simulated ion acoustic waves underscore its robust anti-aliasing properties. Results suggest that this technique may be employed to extend the spectral bandwidth of probe-based plasma wave diagnostics by eliminating aliasing of dispersion data due to the finite separation of probe elements. This technique thus makes possible the experimental detection of small length-scale instability modes existing at wavelengths less than 5 mm, such as the modified two-stream instability, lower hybrid drift instability, and electron cyclotron drift instability.

I. Introduction

HALL thrusters are widely employed electric propulsion (EP) devices that generate thrust by producing and accelerating ions in a cross-field plasma [1]. Recent advances in magnetic shielding (MS) have significantly extended the lifetime of these devices, enabling their use for deep-space applications. However, there remain life-limiting processes that still pose a risk [2]. In particular, wear testing of MS Hall thrusters has revealed a new erosion phenomenon characterized by grating and roughening of magnetic pole surfaces [3]. Consequently, with the advent of MS, “pole erosion” has superseded discharge channel erosion as the primary life-limiting mechanism of these devices.

Recent studies have suggested that this outstanding erosion process may in part be attributed to the onset of plasma instabilities near the inner front pole [4]. The key suspected drivers are the lower hybrid drift instability (LHDI) and the modified two-stream instability (MTSI) which can locally heat ions to sufficiently high energies to sputter the poles [5–7]. However, despite concerted efforts to investigate these instabilities in EP devices, a comprehensive understanding of the modes - and by extension how they may be quenched - has yet to be achieved. This in large part stems from the fact that the wavelengths corresponding to the highest growth rate of these waves lie in a “no man’s land” between 1 and 5 mm, which has been prohibitive to access experimentally. Aliasing effects arising from the finite spacing between wave probe elements impose a lower bound on the wavelengths ($\gtrsim 5$ mm) that physical probe-based methods can resolve [8, 9]. In contrast, optical techniques for measuring wave properties, such as Coherent Thompson Scattering (CTS), have inherent *upper bounds* in spectral bandwidth ($\lesssim 1$ mm) [10, 11]. In light of these outstanding limitations, there is an apparent need to develop a novel diagnostic technique that allows for an expansion of the resolvable wavelength regime to enable experimental measurements of these moderate-wavelength modes.

The goal of this work is to demonstrate a novel anti-aliasing technique based on Bayesian inference that addresses this need. To this end, this paper is structured as follows: in Section II we provide a description of the anti-aliasing algorithm and an overview of Beall analysis, a conventional wave-probe analysis technique against which we validate our algorithm. In section III we detail the methodology used to generate numerical toy data we use to benchmark the two algorithms. In section IV we provide a comparison of the results produced by our anti-aliasing algorithm and Beall analysis, followed by a discussion of our findings in section V. Finally, in section VI we present a summary of the work and key conclusions drawn.

II. Analysis Techniques

We detail in this section two analysis techniques for inferring the dispersion of waves measured using two-probe correlation. The first is an analysis method developed by Beall et al. which yields a histogram of wave dispersion through the frequentist binning of wavenumber-frequency pairs extracted from data taken at a single probe orientation

*PhD Candidate, Department of Aerospace Engineering, Student Member AIAA

† Associate Professor, Aerospace Engineering, Associate Fellow AIAA

[12]. The second is a novel analysis method that leverages Bayesian inference and uses multiple data sets taken at various probe orientations (spacings and/or angles) to arrive at a de-aliased probability distribution of dispersion.

A. Beall analysis

The Beall method produces a histogram of wave dispersion by exploiting phase information encoded in the Fourier transforms of plasma potential fluctuations taken at a pair of spatially separated probes. This technique has been employed in the context of Hall thrusters such as in the works of Brown et al. and Jorns et al. [8, 13]. To illustrate this technique, we show in Fig. 1 a notional schematic of the typical two-probe configuration and corresponding spectral data used to infer wave dispersion.

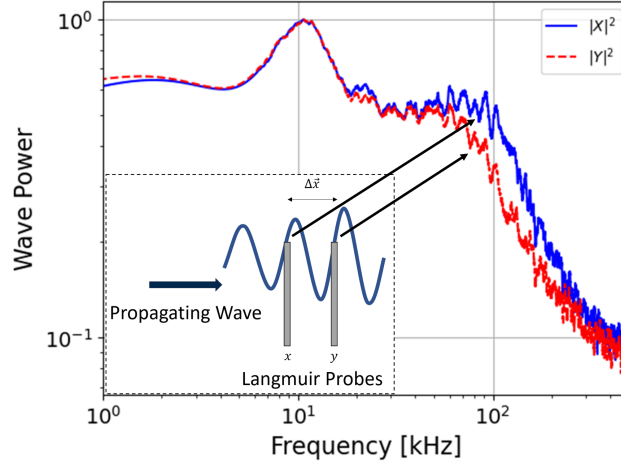


Fig. 1 Notional diagram of two-probe correlation technique.

As a first step, a pair of ion saturation probes (shown in the lower left in Fig. 1) is inserted into a plasma at two positions, x and y , separated by a distance $\Delta\vec{x}$. Electrostatic waves propagating in the plasma will produce phase-separated, time-varying plasma potential fluctuations, $\tilde{\phi}(x, t)$ and $\tilde{\phi}(y, t)$, where $y = x + \Delta\vec{x}$. Following the formulation given in [9], the Fourier transforms of these signals, X_f and Y_f , respectively, can be manipulated to extract the phase difference $\delta\Theta_f$ of waves and thus solve for the wavenumber (wavenumber is proportional to inverse wavelength) $k_{\Delta\vec{x}}(f)$ along the axis connecting the two probe elements as a function of frequency f . The maximum resolvable wavenumber is dictated by the inter-probe spacing, $|k_{max}| \leq \pi/\Delta\vec{x}$:

$$k_{\Delta\vec{x}}(f) = \frac{1}{\Delta\vec{x}}\delta\Theta_f = \frac{1}{\Delta\vec{x}}\tan^{-1}\left[\frac{\mathcal{I}m(Y_f X_f^*)}{\mathcal{R}e(Y_f X_f^*)}\right]. \quad (1)$$

The superscript “*” denotes complex conjugated quantities. As noted in [9], to condition against stochastic noise and identify the dominant modes of fluctuations, Beall et al. proposed a weighted binning of wavenumber-frequency pairs obtained from Eqn. 1 given by

$$S(f_i, k_j) = \frac{1}{M} \sum_{m=1}^M I_{0,\Delta k}[k^j - k^m(f_i)] \frac{1}{2} [P_1^m(f_i) + P_2^m(f_i)]. \quad (2)$$

Here the frequency-wavenumber space is divided into $i \times j$ discrete “bins” where the bin width spans a range of wavenumbers $k_j + \Delta k$ and the bin height spans a range of frequencies $f_i + \Delta f$. Δf is determined by the frequency resolution of data while Δk is specified by the user. M denotes the total number of spectra collected from M pairs of time-varying fluctuation traces, and m denotes the sample index, i.e. the trace number. P_1 and P_2 are the power spectra of fluctuations measured at x and y , respectively, i.e. XX^* and YY^* , and $I_{0\Delta k}$ is an indicator function governed by

$$I_{0\Delta k}[x] = \begin{cases} 1 & \text{if } |x| < \Delta k \\ 0 & \text{otherwise.} \end{cases} \quad (3)$$

$S(f_i, k_j)$ represents the ‘‘intensity’’ value of bin (i, j) which is proportional to the number of samples that fall within each bin weighted by the average of the power spectra. In principle, iterating through every sample m , across every frequency i and wavenumber j , and applying the binning method described by Eqns. 2 and 3 we obtain a heat-map of S as a function of frequency and wavenumber. Larger values of S indicate frequency-wavenumber pairs that are dominant in the measurement domain.

B. Aliasing of Beall dispersion plots

It is evident from Eqn. 1 that the weakness of Beall analysis lies in the $[-\pi, \pi]$ domain restriction of the arctan function. This constraint imposes a maximum resolvable wavenumber determined by the spacing of the probe element where modes with wavenumbers greater than this limit are ‘‘phase-wrapped’’ to fit within the domain. This introduces the issue of aliasing where modes with sufficiently high wavenumber are subject to phase-wrapping and become indistinguishable from non-phase-wrapped, low wavenumber modes. Jorns et al. were able to mitigate this in their work by reconstructing a de-aliased plot given the apparent periodicity of the Beall plot [9]. While this technique is effective at de-aliasing Beall plots with simple, linear dispersion, as in the case of the aforementioned work, various instabilities in Hall thrusters exhibit nonlinear dispersion. Additionally, de-aliasing using this technique is most effective when a single, dominant mode is present. However, depending on the region probed, multiple instabilities may coexist in a Hall thruster plasma. Overlapping dispersion plots will manifest if none of the modes are sufficiently dominant. This, coupled with aliasing uncertainty has made it challenging to apply this de-aliasing technique to nonlinear dispersion measurements in Hall thrusters [14].

C. Bayesian framework

The approach to anti-aliasing presented in this work is predicated on the principle that varying the probe spacing or probe angle will lead to a unique change in the phase difference measured by a probe pair. This invites the possibility that, given data taken at a sufficient number of probe geometries, i.e. angle/spacing combinations, we may simultaneously leverage multiple datasets using Bayesian inference to regress a probability distribution of the true wavenumbers. We briefly overview the principle of Bayesian inference here.

In the Bayesian paradigm, we treat parameters of interest θ as a probability distribution. Given data \mathcal{D} and a model \mathcal{G}_{model} , which relates the parameters θ to data \mathcal{D} , the distribution of parameters conditioned on data, $P(\theta|\mathcal{D})$, i.e. the posterior distribution, is given by

$$P(\theta|\mathcal{D}) = \frac{\mathcal{L}(\mathcal{D}|\theta)P(\theta)}{P(d)} \quad (4)$$

per Baye’s rule. $P(\theta)$ is the prior distribution which represents our belief of what the distribution of θ is prior to observing data. $\mathcal{L}(\mathcal{D}|\theta)$ is the likelihood distribution which represents the probability of observing the data given that θ are the true parameters. $P(d)$ is a normalizing constant computed by marginalizing the likelihood distribution over all θ . This can be interpreted as the marginal probability of observing the data. We note that, for simplicity, the parameters of interest in this work are the 2D wave vectors of propagating modes, i.e. $\theta = (k_{x_1}, k_{x_2})$, which we can learn from datasets obtained by varying probe spacings and angles on only one plane. However, this analysis can be extended to include inference of the wavenumber k_{x_3} in the third dimension by including data taken from probe geometries along a third axis.

We first define the data $\Delta\Theta_f$ as the average of M experimentally measured phase differences $\delta\Theta_f$ for a particular mode with frequency f , i.e. $\Delta\Theta_f = \mathbb{E}[\delta\Theta_f]$. Next, we define our model relating parameters to measured data as

$$\mathcal{G}_f(k_{x_1}, k_{x_2}; \Delta\vec{x}) = \vec{k}(f) \cdot \Delta\vec{x} + \xi, \quad \xi \sim \mathcal{N}(0, \sigma_{\delta\Theta_f}^2), \quad (5)$$

where $\mathcal{G}_f(k_{x_1}, k_{x_2}; \Delta\vec{x})$ can be related to the wave vector \vec{k} and ‘‘probe vector’’ $\Delta\vec{x}$ connecting the probe elements with respect to a user-defined, common axis. To encode measurement noise and uncertainty, we endow the model with Gaussian noise ξ distributed with zero mean and variance $\sigma_{\delta\Theta_f}^2$ equal to the variance of experimental measurements of $\delta\Theta_f$, i.e. $\sigma_{\delta\Theta_f}^2 = \text{Var}[\delta\Theta_f]$. Using this model, the Gaussian likelihood for one probe orientation is given by

$$\mathcal{L}(\Delta\Theta_f|k_{x_1}, k_{x_2}; \Delta\vec{x}) = \frac{1}{2\pi\sigma_{\delta\Theta_f}} \exp\left(-\frac{1}{2} \frac{(\Delta\Theta_f - \mathcal{G}_f(k_{x_1}, k_{x_2}; \Delta\vec{x}))^2}{\sigma_{\delta\Theta_f}^2}\right). \quad (6)$$

Here $\mathcal{G}_f(k_{x_1}, k_{x_2}; \Delta\vec{x})$ is the model output for the phase change we expect to observe for a particular probe configuration $\Delta\vec{x}$ given the input parameters (k_{x_1}, k_{x_2}) are the true wavenumbers. The likelihood function decreases as the model outputs deviate from the experimentally observed data and increases as they align more closely. Consequently, the likelihood function is maximized when the input parameters match the "true" parameters that produced the experimental data. However, due to aliasing, which results in phase-wrapped data, measurements from a single probe geometry are insufficient to infer the true wavenumbers. In other words, all $\pm 2\pi$ "harmonics" of the true wavenumber will all equally maximize the likelihood. In light of this, we modify our likelihood function to incorporate data from a set of n probe geometries $[\Delta\vec{x}_1 \dots \Delta\vec{x}_n]$, where each probe vector $\Delta\vec{x}$ is defined with respect to a common axis,

$$\mathcal{L}_f(\Delta\Theta_f^i | (k_{x_1}, k_{x_2}); [\Delta\vec{x}_1 \dots \Delta\vec{x}_n]) = \prod_{i=1}^n \frac{1}{2\pi\sigma_f^i} \exp\left(-\frac{1}{2} \frac{(\Delta\Theta_f^i - \mathcal{G}_f^i(k_{x_1}, k_{x_2}; \Delta\vec{x}_i))^2}{(\sigma^2)_f^i}\right). \quad (7)$$

In lay terms, under the assumption of independently and identically distributed data, we posit that the true wavenumbers will maximize the product of the likelihoods across all probe geometries. In principle, with sufficient number of small angle and spacing variations, even if the data is aliased in one direction, the particular combination of $\Delta\Theta_f$ associated with the set of probe geometries will be largely unique to one wave vector. We may then perform a parametric grid search of wave vectors to obtain the likelihood distribution.

If we elect to employ a uniform prior distribution, the likelihood distribution represents an unnormalized posterior distribution. If we are purely interested in the most probable regions of wave dispersion relative to other regions on the domain, as in this case, this unnormalized probability distribution function (PDF) is sufficient; there is no need to normalize the PDF by computing the evidence. Additionally, we note here that this unnormalized PDF may be employed in Bayesian Markov Chain Monte Carlo (MCMC) algorithms for approximating the normalized posterior distribution [15, 16]. To this point, MCMC is a more suitable technique for inferring three-dimensional dispersion as the computational expense of grid search scales poorly with the number of parameters.

D. Anti-aliasing algorithm

We show in Fig. 2 below an overview of the anti-aliasing data analysis process.

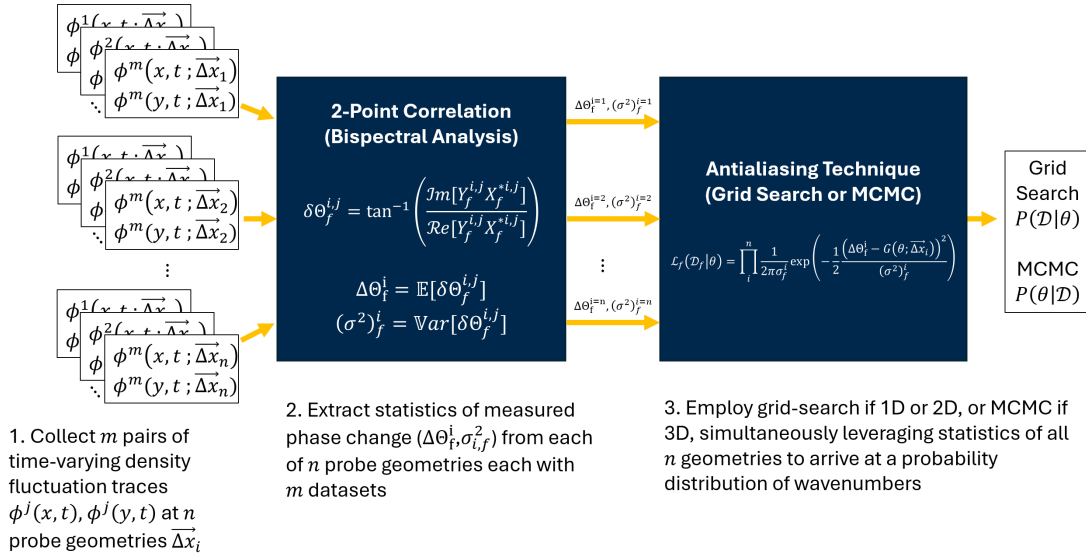


Fig. 2 General procedure for anti-aliasing approach

We begin by obtaining a statistically sufficient m number of time-varying probe-pair traces for each of n probe orientations. Next, we divide the frequency domain into F frequencies. For each frequency f and probe geometry $\Delta\vec{x}_i$, we generate a histogram using m samples of $\delta\Theta_f^i$ from which we extract the mean, $\Delta\Theta_f^i = \mathbb{E}[\delta\Theta_f^{i,j}]$, and variance $(\sigma^2)_f^i = \text{Var}[\delta\Theta_f^{i,j}]$. Here, samples are indexed by the superscript j and the probe geometries are indexed by the superscript i . Due to phase-wrapping (detailed in the preceding subsection) careful treatment is required to ensure we

obtain statistics that are representative of the true distribution. We discuss this in the following section. The likelihood function incorporates the mean and variance from all n histograms corresponding to a given frequency. In this work we use grid search where, for each frequency index, we sweep the input parameters $\theta = k_{x_1}, k_{x_2}$ across a range of wavenumbers to generate a heat map of the likelihood as a function of k_{x_1} and k_{x_2} . For 3D dispersion, MCMC can be used instead.

E. Extracting histogram statistics

Given the possibility of phase-wrapping, statistics cannot be blindly extracted from histograms of phase data. We illustrate this with the following, notional example in Fig. 10. Suppose a mode with wavenumber $k \cong k_{max}$ is aliased such that the "true" distribution (shown in purple) of phase difference measured by the probe pair is approximately centered about π . Given the domain restriction of the arctan function, bispectral analysis will instead produce the phase-wrapped distribution (orange). It is evident that if we were to blindly extract statistics from this histogram without accounting for phase-wrapping, we will mistakenly extract a mean phase of approximately 0 and a large variance. This would be grossly unrepresentative of the true distribution. In light of this, we propose the following algorithm to extract close estimates of the true histogram statistics.

- 1) Set the bin width of the histogram (hyperparameter)
- 2) Take the mode, $\text{argmax}[f(\delta\Theta)]$, of the histogram as an estimate for the mean
- 3) Phase shift the distribution such that $\text{argmax}[f(\delta\Theta)]$ is centered about 0 through the following:
 - a) If $\text{argmax}[f(\delta\Theta)] > 0$
 - i) subtract $\text{argmax}[f(\delta\Theta)]$ from all phases ($\delta\Theta$) that satisfy $\delta\Theta \geq \text{argmax}[f(\delta\Theta)] - \pi$
 - ii) subtract $\text{argmax}[f(\delta\Theta)]$ and add 2π to all phases that satisfy $\delta\Theta < \text{argmax}[f(\delta\Theta)] - \pi$
 - b) If $\text{argmax}[f(\delta\Theta)] < 0$
 - i) add $-\text{argmax}[f(\delta\Theta)]$ to all phases that satisfy $\delta\Theta \leq \text{argmax}[f(\delta\Theta)] + \pi$
 - ii) add $-\text{argmax}[f(\delta\Theta)]$ and subtract 2π from all phases that satisfy $\delta\Theta > \text{argmax}[f(\delta\Theta)] + \pi$
- 4) Extract the variance σ^2 of the phase-shifted histogram (green distribution in Fig. 3)

Given sufficient samples and Gaussian noise, the histogram should converge to a Gaussian, a symmetric distribution. The mode of the histograms can thus serve as a proxy for the mean. Using this estimate of the mean, we can phase-shift the distribution such that it is centered about zero per step 3 above. We can then compute the variance of this phase-shifted distribution (green), which we see the shape of which is now much more representative of the true distribution.

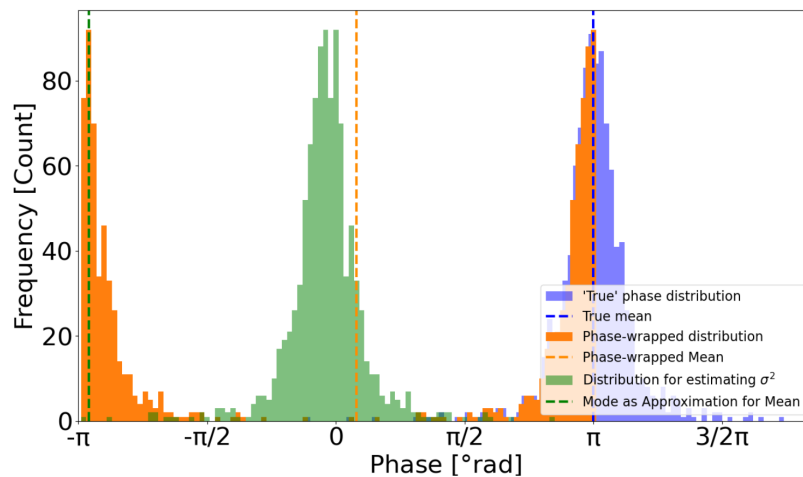


Fig. 3 Comparison of true distribution, phase-wrapped distribution, and distribution used to estimate variance

We show in Tables 1 and 2 a comparison of the estimated statistics with and without conditioning for phase-wrapping. We see from these results that computing the statistics without accounting for phase-wrapping leads to significant deviation of the estimated statistics from their true values.

-	Value	% Err.
True Mean	3.139	0
Phase-wrapped Mean	0.251	92
Mode (phase-corrected)	3.267	4

Table 1 Comparison of histogram means

-	Value	% Err.
True Variance	0.478	0
Phase-wrapped variance	2.849	502
Phase-shift corrected variance	0.473	1

Table 2 Comparison of histogram variances

III. Simulation Methodology

We discuss in this section our methodology for generating and extracting statistics from toy data. We first present the theoretical dispersion of ion acoustic waves which we use to generate simulated spectra associated with these modes. We then describe how we simulate plasma probes and data collection.

A. Simulating spectra of IAT

The ion acoustic instability is an electrostatic mode that arises spontaneously in plasmas with significant disparities in ion and electron temperatures or drift velocities [17–19]. The dispersion relation for ion acoustic waves can be derived from the linear perturbation analysis of the Boltzmann equations for ions and electrons. In light of the fact that the experimentally observed frequencies at which these waves propagate are lower than the ion plasma frequency [9], $\omega_{RE} \ll \omega_{pi}$, the dispersion relation is given by

$$\omega_{RE} = kc_s + \vec{k} \cdot \vec{v}_i. \quad (8)$$

The ion sound speed c_s and ion drift velocity v_i determine the linear slope of the dispersion relation, which is also the group velocity v_g of the waves. We choose to generate simulated ion acoustic waves using this dispersion relation due to its simplicity. We note that, while experimentally observed measurements of the group velocity are of order 10^3 m/s [9, 20], for the purposes of simulating a highly aliased data set to compare Beall analysis against our anti-aliasing algorithm, we set a shallow slope corresponding to a group velocity of approximately 300 m/s. We show in Fig. 4 the resulting dispersion relation from which we can generate this spectra of simulated plasma waves. We note that we set a default group velocity of 2042 m/s for our other results.

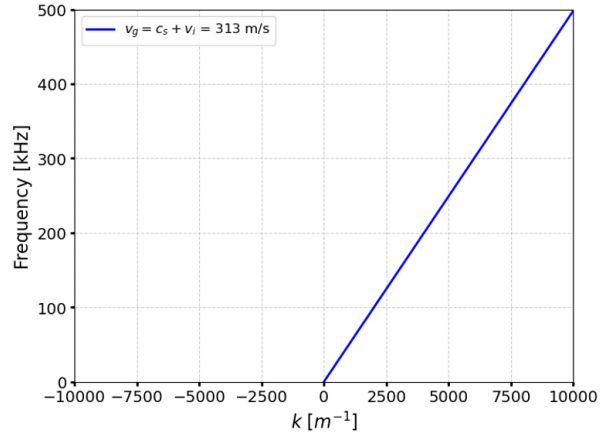


Fig. 4 Linear dispersion used to generate aliased data

B. Simulating wave-probe data collection

Simulated plasma waves are generated per the dispersion relation discussed in the proceeding section for a range of wavenumbers. For each wavenumber, we simulate a plane wave (Fig. 5a) with frequency f determined by the dispersion relation. We then insert two “virtual” probes (Fig. 5b) into the domain and simulate the contribution to the time-varying signal that would be collected by the probes as the plane wave propagates (Fig. 5c). We model the total time-varying signal measured by the probes as

$$\phi(x, t) = \sum_{f=1}^F A \sin(-\omega_f \cdot t) + \xi(t), \quad \xi \sim \mathcal{N}(0, \Gamma) \quad (9)$$

and

$$\phi(y, t) = \sum_{f=1}^F A \sin(\vec{k}_f \cdot \vec{r} - \omega_f \cdot t) + \xi(t), \quad \xi \sim \mathcal{N}(0, \Gamma). \quad (10)$$

Here A is the amplitude of the wave, which we set to unity. ω_f is the angular frequency of the wave mode which can be calculated as $\vec{k}_f \cdot \vec{v}_g$, where \vec{v}_g is the group velocity of the waves. As discussed in the proceeding section, we prescribe the value of \vec{v}_g to the dispersion relation in this work. The index f denotes the f^{th} wavenumber (corresponding to frequency f) in our wavenumber range of interest. $\vec{r} = (r_{x_1}, r_{x_2})$ is the position vector of the probe y , where $r_{x_1} = \Delta x \cdot \sin(\theta_{probe})$ and $r_{x_2} = \Delta x \cdot \cos(\theta_{probe})$ are calculated from the probe spacing, Δx , and the angle, θ_{probe} , that $\Delta \vec{x}$ makes with respect to the positive x_2 axis. Γ is the variance of the random Gaussian noise. Fig. 5 shows notionally an example of the simulated data generated by one particular mode k_f propagating solely in the x_2 direction with wavenumber $k = 1000 [m^{-1}]$ where the noise variance is set to 0. Fig. 6 shows an example of a possible probe orientation and the corresponding simulated data generated.

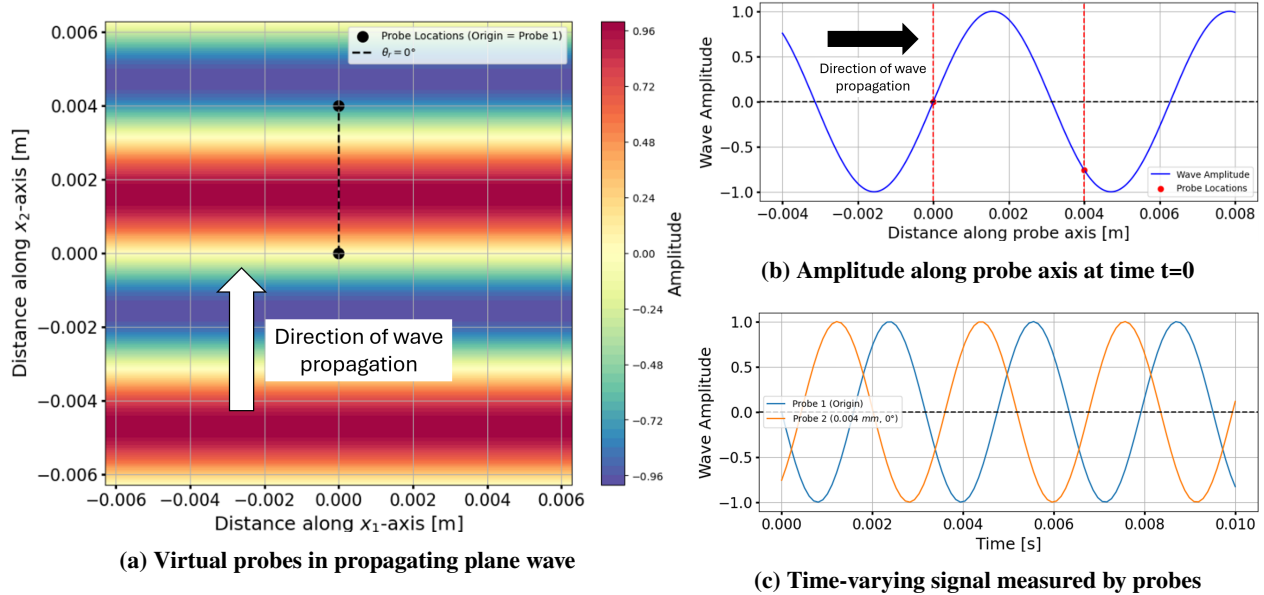


Fig. 5 Simulated data from probes aligned with wave vector

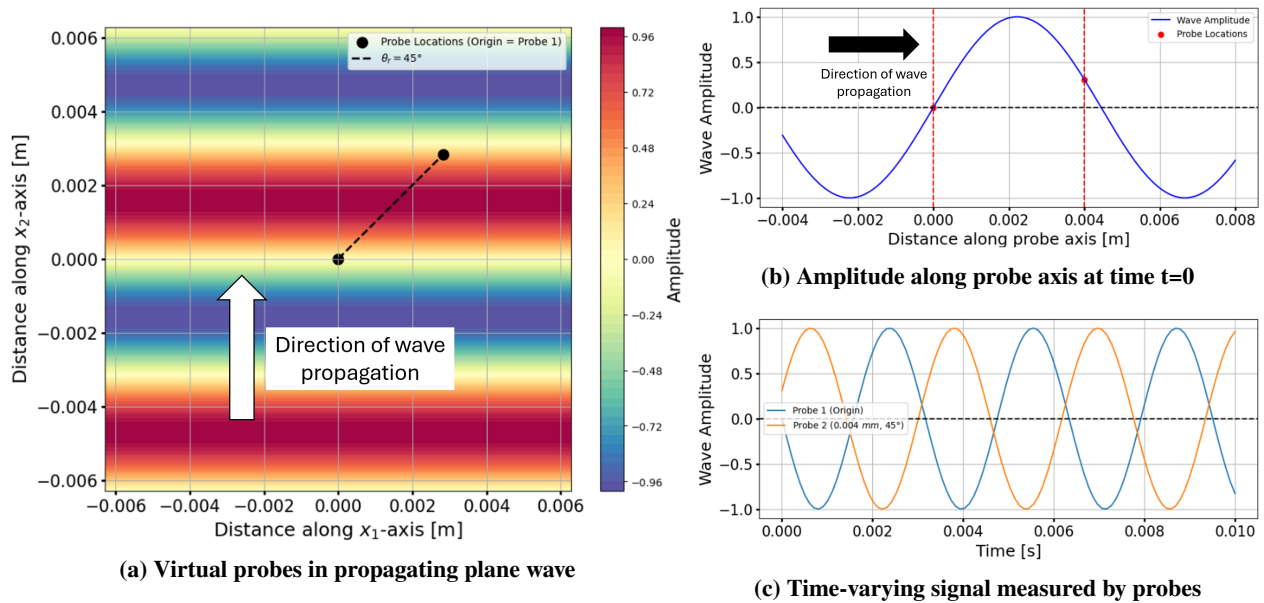


Fig. 6 Simulated data from probes angled 45° with respect to wave vector

To generate a “realization” of time-varying data for one probe configuration $(\vec{r}, \theta_{probe})$, we first prescribe a sampling duration T and sampling time interval Δt . We then propagate Eqns. 9 and 10, the dynamics, forward in time in increments of Δt up to T . At every time step, we sum the wave amplitude of F modes, each of which is perturbed by random Gaussian noise. One realization of data is thus a data vector of length $T/\Delta t$ where each element corresponds to the sum of wave amplitudes at each time step. Following the process given in Fig. 2 and Eqns. 9 and 10, we generate M realizations of the sum of F plane waves spanning a range of wavenumbers, perturbed by Gaussian noise. We show in Fig. 7 example realizations of data sampled over 2 ms with $\Delta t = 1\ \mu\text{s}$ and noise variance $\Gamma = 5$ (Fig. 7a) and $\Gamma = 50$ (Fig. 7b). We can further divide these traces into L segments to arrive at an $m = M \times L$ effective number of realizations.

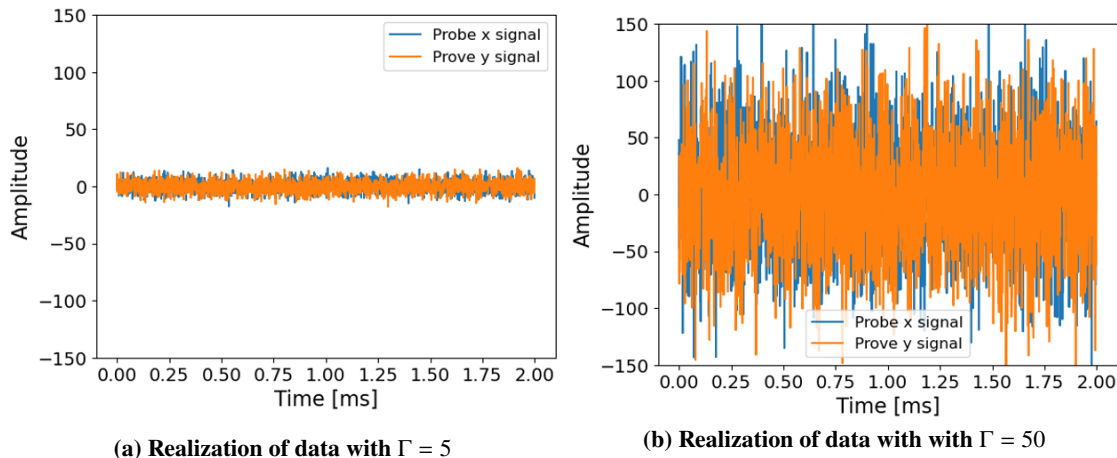


Fig. 7 Realization of data with different noise variances

Next, we Fourier transform these realizations and extract the phase data through bispectral analysis following Eqn. 1. We repeat this process for n number of probe geometries. We ultimately arrive at $m \times n$ number of spectra from which we can extract phase information.

IV. Results

We present in this section results for validating our algorithm. We first show the outcomes of units tests demonstrating the scaling of the anti-aliasing technique with the number of data sets taken. We then detail the effect of spacing step-size on the likelihood function. Finally, we provide a comparison across a range of signal-to-noise ratios of the dispersion histogram produced through conventional two-point correlation Beall analysis with the dispersion probability distribution produced using the anti-aliasing technique.

A. Probe geometry convergence study

We show in Fig. 8 the effect of various probe spacing and angle combinations on the likelihood function (Eqn. 7). The plots shown here are each for a single mode with wave vector (k_{x_1}, k_{x_2}) . We tabulate the particular set of spacings and angles for each probing combination in this study in Table 3. We also show the corresponding combination of probe orientations to the right of each plot. For each probe geometry, we generate 100 realizations of simulated spectra with noise $\Gamma = 0.5$. For example, for 5 spacings, a total of 500 realizations are generated, 100 per probe pair. The group velocity of the waves in this study is set to 2042 m/s . The wave vector of the particular mode interrogated in the plots of Fig. 8a is $(k_{x_1}, k_{x_2}) = (0, 120)$. The wave vector of interest in the plots of Fig. 8b is $(k_{x_1}, k_{x_2}) = (1060, 1060)$.

The first plot of Fig. 8a (“1 spacing”) illustrates the issue of aliasing encountered in Beall analysis. All $\pm 2\pi$ harmonics of the wavenumber are equally likely. We see from the plots of Fig. 8a that, although increasing the number of spacings will de-alias the data in one direction, multiple spacings alone are insufficient to identify the 2D wave vector. This is physically intuitive as probing solely in one direction will only yield information about the wavenumber along that axis. There remains uncertainty in the wavenumber along the other axis. This is reflected in the likelihood plots of Fig. 8a where all wavenumbers in the x_1 direction are equally likely. We see from Fig. 8b that combining spacing variations with angle variations can reveal the full wave vector. As additional data is incorporated from multiple geometries, the likelihood plot becomes increasingly peaked in the vicinity of the true wave vector.

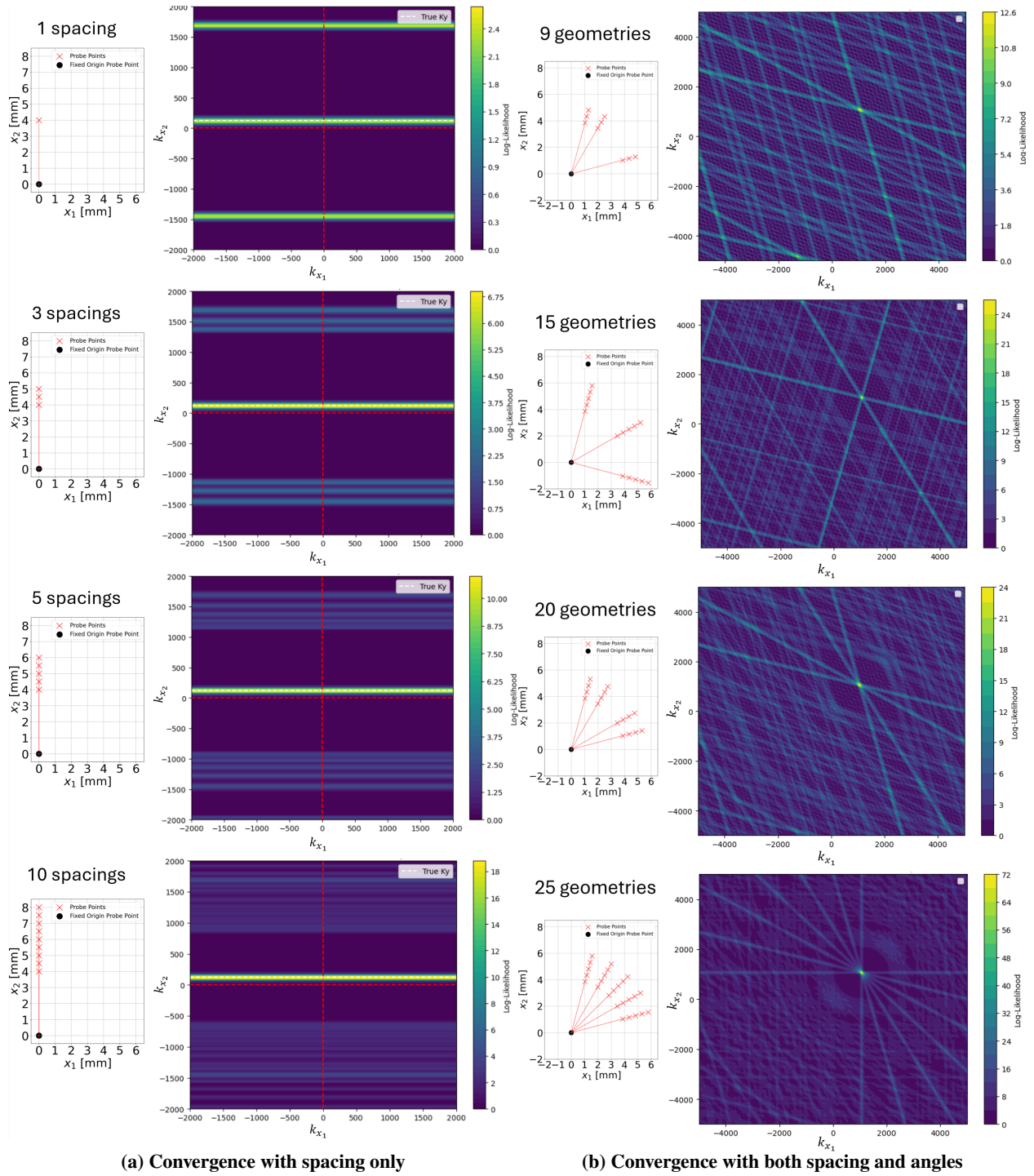


Fig. 8 Convergence of likelihood plots- with various probe geometries

Plot	Spacings (mm)	Angles (°)
1 spacing	4	0
3 spacings	4, 4.5, 5	0
5 spacings	4, 4.5, 5, 5.5, 6	0
10 spacings	4, 4.5,... 8.5	0
9 geometries	4, 4.5, 5	15, 30, 75
15 geometries	4, 4.5, 5, 5.5, 6	15, 60, 105
20 geometries	4, 4.5, 5, 5.5, 6	15, 30, 60, 75
25 geometries	4, 4.5, 5, 5.5, 6	15, 30, 45, 60, 75

Table 3 Convergence study probing geometries

B. Effect of spacing step-size on likelihood distribution

We show in Fig. 9 the effect of smaller step sizes on the outputs of the anti-aliasing algorithm. Here we compare spacing increments of 0.5 mm and 0.1 mm. We show the particular probe geometries used to the right of each plot. We generate 100 realizations of simulated spectra for each spacing with noise $\Gamma = 0.5$. In this study, the group velocity of the waves is set to 2042 m/s. The wave vector of the particular mode interrogated in Fig. 9 is $(k_{x_1}, k_{x_2}) = (0, 1500)$.

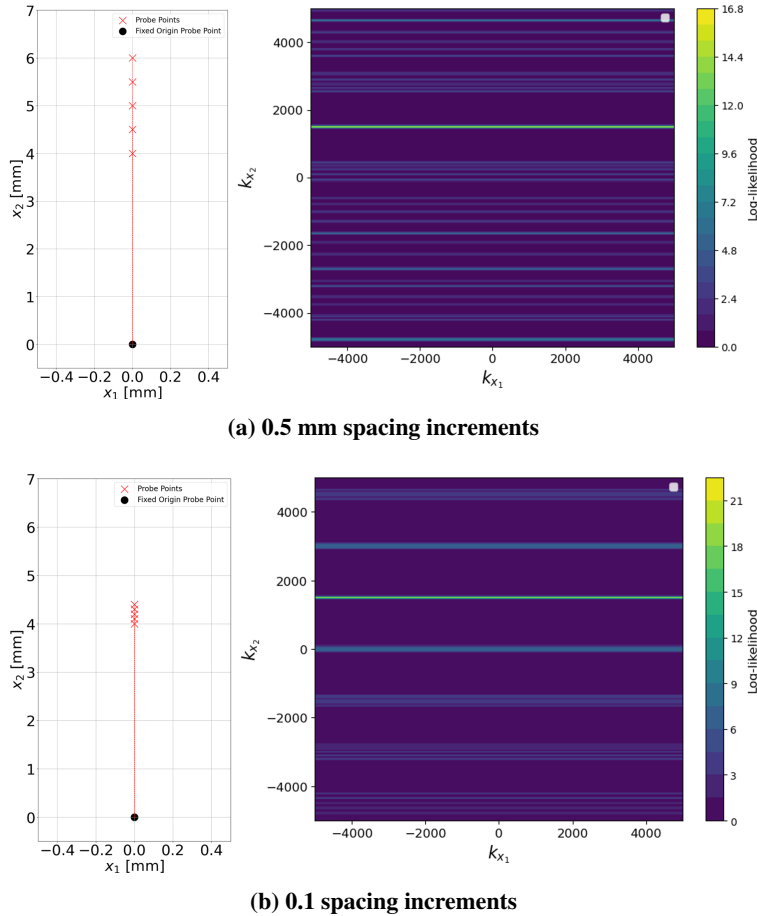


Fig. 9 Effect of spacing step size on likelihood plot

It is evident from this result that, for the same number of probe geometries, finer spacing produces a more highly peaked likelihood function. This is a physically intuitive result. A finer spacing allows for the evaluation of finer changes in phase. In this manner, finer spacing increments is analogous to closer inter-probe spacing of probe elements.

C. Comparison of Beall analysis plots with anti-aliasing likelihood distributions

We show in Fig. 10 the key result of this work where we directly compare the dispersion histogram produced from Beall analysis with the probability distribution of dispersion produced by our anti-aliasing algorithm across a range of signal-to-noise ratios (SNR). SNR of simulated data is calculated as

$$SNR = \frac{\langle P_{wave} \rangle}{\langle P_{noise} \rangle} = \frac{0.5A_{wave}^2}{\Gamma}, \quad (11)$$

the average wave power over the variance of the noise. Given a wave amplitude A of unity, we set SNR by changing the variance of the Gaussian noise parameter. SNR is denoted above each plot. The probe geometries of each technique is tabulated below in Table 4 and illustrated in the bottom left of each sub plot.

Analysis Technique	Spacings (mm)	Angles (°)
Beall method	4	0
Antialiasing algorithm	4, 4.5, 5, 5.5, 6	15, 30, 45, 60, 75

Table 4 Probe geometries used in algorithm comparison

We generated 1000 realizations of simulated spectra for each probe orientation. As discussed in section III, to produce highly aliased data, the group velocity of the waves is set to 313 m/s. The Beall method only leverages data from one probe pair. In contrast, the anti-aliasing algorithm leverages 25 datasets from 5 different spacings and angles. We see from Fig. 10a that the dispersion plot produced from Beall analysis exhibits severe aliasing characterized by multiple parallel striations. In comparison, the likelihood distribution of dispersion generated using the anti-aliasing algorithm exhibits no aliasing and correctly reconstructs the wave dispersion across the entire wavenumber range. We see from the SNR sweep that the robustness of the anti-aliasing algorithm to noise is comparable to that of Beall analysis. With 1000 realizations of data taken at each probe orientation, the SNR limit of both techniques appears to be around 1:10. At an SNR of 1:20 both techniques produce plots with no discernible dispersion. We note that the maximum SNR will increase if more data are taken.

V. Discussion

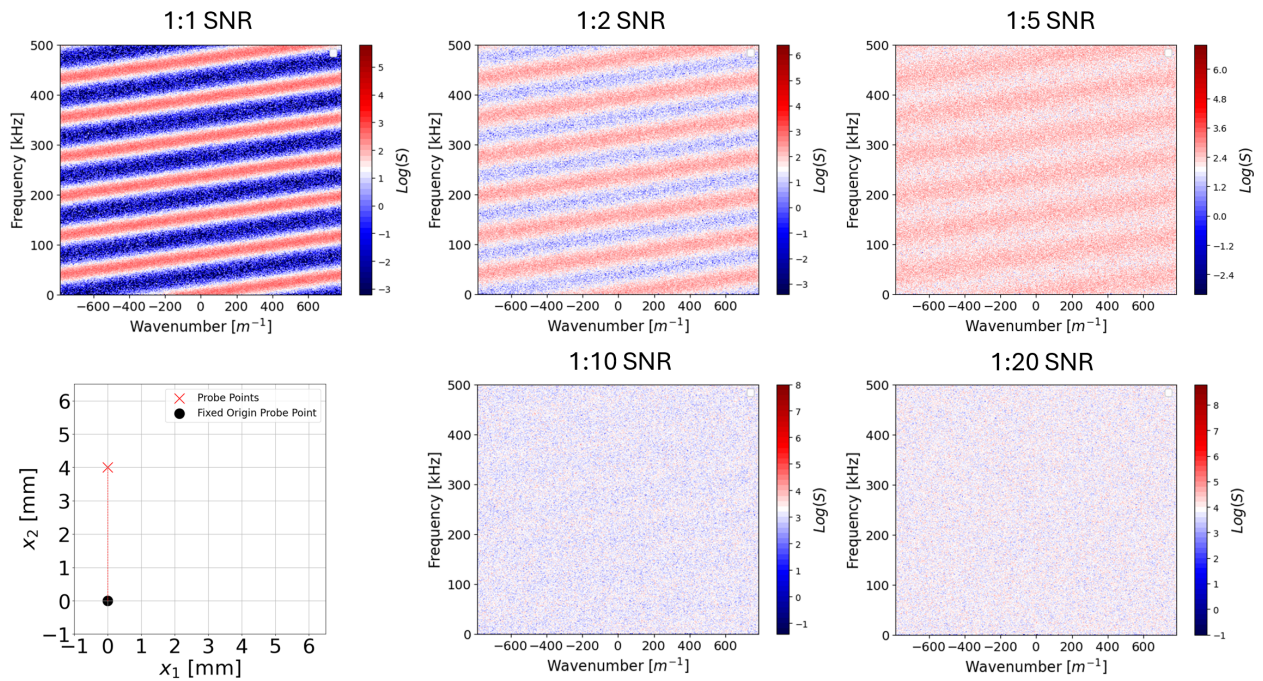
We discuss in this section some limitations of the validation work and possible future extensions of the validation effort. We additionally discuss some considerations for experimentally implementing this technique.

A. Limitations of this validation work

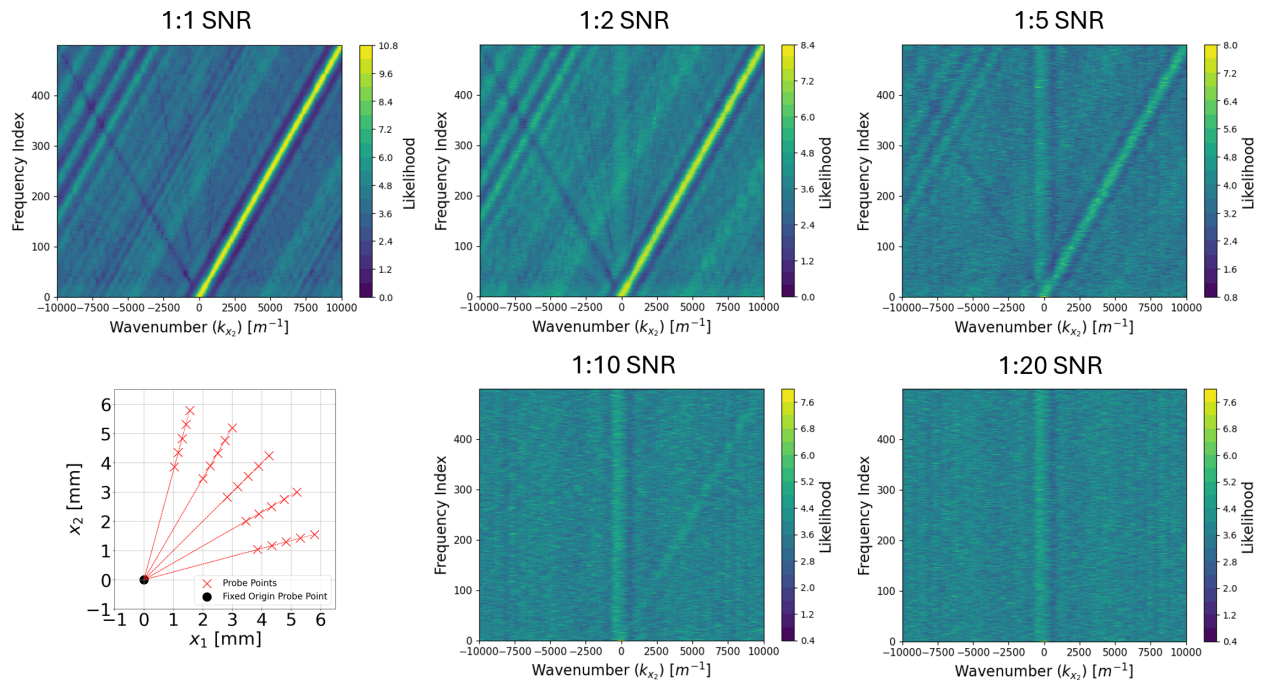
While the results presented in the proceedings sections are promising, several limitations in the validation process warrant discussion. First, the method was validated using a simple linear dispersion relation. Although the technique should, in principle, be applicable to nonlinear dispersion relations, further validation is required to confirm its viability in such scenarios. Second, we model plasma waves as unidirectional 2D plane waves. In reality, plasma waves are inherently three-dimensional. Future validation work will include an extension of this algorithm to three dimensions.

Our plane wave model also assumes that the wave vector of a propagating mode remains constant across all probing geometries, i.e. the wave vectors are independent of position. This assumption allows us to project all probe vectors onto the same wave vector for computing phase change. However, the wave vectors of a mode in real EP plasmas may be spatially dependent even when the wave vector magnitude remains the same. For example, a single ion acoustic mode propagating outward in a hollow cathode plume could have wave vectors that vary with position. Under such conditions, the anti-aliasing algorithm could yield inaccurate wave vector reconstructions. To address this issue, we can probe at sufficiently small spatial increments such that wave vectors can reasonably be assumed to vary negligibly across probe geometries. In other words, we posit that the waves will appear locally plane-wave-like across sufficiently small spatial scales. This approach synergizes well with our findings that finer probe spacing/angle adjustments improve algorithm performance. Alternatively, we can explore methods to incorporate wave vector variability directly into the Bayesian inference framework.

Finally, due to the computational expense associated with data generation and simulation, we validated this technique using only 1000 realizations of data per orientation. By contrast, experimental studies employing bispectral analysis often incorporate thousands or even tens of thousands of realizations. However, we note that increased data generally decreases the impact of noise. Thus, the algorithm's effectiveness should only improve given more data.



(a) Beall plots showing severe aliasing



(b) Anti-aliasing likelihood plots showing no aliasing

Fig. 10 Comparison of dispersion plot produced by analysis techniques at varying SNR

B. Experimental implementation

Employing this analysis experimentally requires designing a probe array capable of adjusting both the probe spacing and probe angle in situ. This is comparatively more complex to implement than a simple, fixed probe pair used for Beall analysis. However, a key advantage of this technique is its ability to potentially mitigate the effects of probe shadow shielding [20] by utilizing multiple probe orientations. In principle, even if shadow shielding significantly affects one geometry, the impact may be effectively “averaged out” across other geometries and thus mitigated. Additionally, since the influence of probe shielding diminishes with increasing inter-probe distances [21], we can collect data at a larger initial probe spacing. While spacing probe elements farther apart typically reduces the maximum detectable wavenumber and exacerbates aliasing, our technique inherently corrects for aliasing and thus avoids this associated penalty.

Given this technique is predicated on achieving particular probe geometries with high accuracy, it is important to consider the spatial resolution and precision of the motion stages used in the construction of the probe array. If the positional accuracy is sufficiently low, then probe spacing and angle variability will likely need to be incorporated as additional parameters in the Bayesian inference framework to rigorously account for this uncertainty. The variability can be reduced with the use of high-precision stepper motors and encoders.

Lastly, we note that although we have presented this analysis method in the context of physical probes, it can in principle be extended to optical techniques, provided time-varying plasma density fluctuations at multiple locations in the plasma can be measured. This can potentially be done through passive high-speed imaging and LIF [22].

VI. Conclusion

In this work, we validated a novel wave analysis technique capable of reconstructing wave dispersion from aliased data by leveraging multiple data sets through Bayesian inference. Our results show that the performance of the algorithm improves with greater data availability and finer probe spacing. When compared directly to a conventional two-point correlation Beall bispectral analysis, the new anti-aliasing multi-point correlation technique successfully reconstructs dispersion without aliasing. Our finding suggests that this new technique can be leveraged to obtain the first experimental measurements of small-length-scale fluctuations that have been to date inaccessible to conventional probing techniques due to aliasing.

Acknowledgments

This work was supported by a NASA Space Technology Graduate Research Opportunity (NSTGRO) Fellowship (80NSSC24K1331), the University of Michigan Rackham Graduate School Rackham Merit Fellowship (RMF), and the U.S. Department of Energy, Office of Science, Office of Fusion Energy Sciences, under the Early Career Research Program Award, DE-SC0022988.

References

- [1] Goebel, D. M., Katz, I., and Mikellides, I. G., *Fundamentals of Electric Propulsion*, Wiley, New Jersey, 2024. Chapter 7: Conventional Hall Thrusters.
- [2] Mikellides, I., Katz, I., Hofer, R., and Goebel, D., *Design of a Laboratory Hall Thruster with Magnetically Shielded Channel Walls, Phase III: Comparison of Theory with Experiment*, 48th AIAA/ASME/SAE/ASEE Joint Propulsion Conference Exhibit, 2012. <https://doi.org/10.2514/6.2012-3789>, URL <https://arc.aiaa.org/doi/abs/10.2514/6.2012-3789>.
- [3] Frieman, J. D., Kamhawi, H., Peterson, P. Y., Herman, D. A., Gilland, J. H., and Hofer, R. R., *Completion of the Long Duration Wear Test of the NASA HERMeS Hall Thruster*, AIAA Propulsion and Energy 2019 Forum, 2019. <https://doi.org/10.2514/6.2019-3895>, URL <https://arc.aiaa.org/doi/abs/10.2514/6.2019-3895>.
- [4] Ortega, A. L., Mikellides, I. G., Chaplin, V. H., Huang, W., and Frieman, J. D., *Anomalous Ion Heating and Pole Erosion in the 12.5-kW Hall Effect Rocket with Magnetic Shielding (HERMeS)*, AIAA Propulsion and Energy 2020 Forum, 2020. <https://doi.org/10.2514/6.2020-3620>, URL <https://arc.aiaa.org/doi/abs/10.2514/6.2020-3620>.
- [5] Mikellides, I. G., and Lopez Ortega, A., “Growth of the lower hybrid drift instability in the plume of a magnetically shielded Hall thruster,” *Journal of Applied Physics*, Vol. 129, No. 19, 2021, p. 193301. <https://doi.org/10.1063/5.0048706>, URL <https://doi.org/10.1063/5.0048706>.
- [6] Mikellides, I. G., and Ortega, A. L., “Growth of the modified two-stream instability in the plume of a magnetically shielded Hall thruster,” *Physics of Plasmas*, Vol. 27, No. 10, 2020, p. 100701. <https://doi.org/10.1063/5.0020075>, URL <https://doi.org/10.1063/5.0020075>.
- [7] Mikellides, I. G., Lopez Ortega, A., and Chaplin, V. H., “Theory of the anomalous momentum exchange from wave–particle interactions in Hall-effect ion accelerators and comparisons with measurements,” *Physics of Fluids*, Vol. 36, No. 7, 2024, p. 074121. <https://doi.org/10.1063/5.0213605>, URL <https://doi.org/10.1063/5.0213605>.
- [8] Brown, Z. A., and Jorns, B. A., “Spatial evolution of small wavelength fluctuations in a Hall Thruster,” *Physics of Plasmas*, Vol. 26, No. 11, 2019, p. 113504. <https://doi.org/10.1063/1.5116708>, URL <https://doi.org/10.1063/1.5116708>.
- [9] Jorns, B. A., Mikellides, I. G., and Goebel, D. M., “Ion acoustic turbulence in a 100-A LaB6 hollow cathode,” Vol. 90, No. 6, 2014. <https://doi.org/10.1103/PhysRevE.90.063106>.
- [10] Tsikata, S., Lemoine, N., Pisarev, V., and Grésillon, D. M., “Dispersion relations of electron density fluctuations in a Hall thruster plasma, observed by collective light scattering,” *Physics of Plasmas*, Vol. 16, No. 3, 2009, p. 033506. <https://doi.org/10.1063/1.3093261>, URL <https://doi.org/10.1063/1.3093261>.
- [11] Tsikata, S., Hara, K., and Mazouffre, S., “Characterization of hollow cathode plasma turbulence using coherent Thomson scattering,” *Journal of Applied Physics*, Vol. 130, No. 24, 2021, p. 243304. <https://doi.org/10.1063/5.0071650>, URL <https://doi.org/10.1063/5.0071650>.
- [12] Beall, J. M., Kim, Y. C., and Powers, E. J., “Estimation of wavenumber and frequency spectra using fixed probe pairs,” *Journal of Applied Physics*, 1982. <https://doi.org/10.1063/1.331279>.
- [13] Jorns, B., Cusson, S. E., Brown, Z., and Dale, E. T., “Non-classical electron transport in the cathode plume of a Hall effect thruster,” *Physics of Plasmas*, 2020. <https://doi.org/10.1063/1.5130680>.
- [14] Brown, Z., and Jorns, B., “Experimental measurements of the contribution of plasma turbulence to anomalous collision frequency in a Hall thruster,” *AIAA Propulsion and Energy 2021 Forum*, 2021. <https://doi.org/10.2514/6.2021-3415>.
- [15] Hastings, W. K., “Monte Carlo sampling methods using Markov chains and their applications,” *Biometrika*, Vol. 57, No. 1, 1970, pp. 97–109. <https://doi.org/10.1093/biomet/57.1.97>, URL <https://doi.org/10.1093/biomet/57.1.97>.
- [16] Haario, H., Laine, M., Mira, A., and Saksman, E., “DRAM: Efficient adaptive MCMC,” *Statistics and Computing*, 2006. <https://doi.org/10.1007/s11222-006-9438-0>.
- [17] Bychenkov, V. Y., Silin, V. P., and Uryupin, S. A., “Ion-acoustic turbulence and anomalous transport,” *Physics Reports*, 1988. [https://doi.org/10.1016/0370-1573\(90\)90122-i](https://doi.org/10.1016/0370-1573(90)90122-i).
- [18] Stix, T. H., “Waves in plasmas: Highlights from the past and present,” *Physics of Fluids B: Plasma Physics*, Vol. 2, No. 8, 1990, pp. 1729–1743. <https://doi.org/10.1063/1.859444>.
- [19] Swanson, D. G., “Plasma Waves (2nd edition),” *Plasma Physics and Controlled Fusion*, 2003. <https://doi.org/10.1088/0741-3335/45/6/701>.

- [20] Liu, M. F., and Jorns, B. A., “Experimental Measurements of the Dispersion and Growth Rate of Ion Acoustic Waves in the Plume of a Hollow Cathode,” *38th International Electric Propulsion Conference*, 2024.
- [21] Mooney, M. M., and Lemmer, K. M., “The effect of probe separation distance on the analysis of plasma waves in a cathode plasma,” *AIAA SCITECH 2024 Forum*, 2024. <https://doi.org/10.2514/6.2024-0923>.
- [22] Geogin, M. P., Byrne, M., Jorns, B. A., and Gallimore, A. D., “Passive High-speed Imaging of Ion Acoustic Turbulence in a Hollow Cathode,” *53rd AIAA/SAE/ASEE Joint Propulsion Conference*, 2017. <https://doi.org/10.2514/6.2017-4973>.